APPLICATIONS OF REMOTE SENSING IN LITHOLOGICAL MAPPING OF EAST GABAL ATUD AREA, CENTRAL EASTERN DESERT, EGYPT

Maher DAWOUD[1], Ibrahim M. KHALAF[1], Hanaa A. EL- DOKOUNY[1], Ali SHEBL[2,3], Hamdy A. EL-DESOUKY[1,4], Abdelhalim Sh. MAHMOUD[5], Mai A. EL-LITHY[1]

[1]Geology Department, Faculty of Science, Menoufia University, Egypt
e-mail: dawoud_99@yahoo.com
[2]Department of Mineralogy and Geology, University of Debrecen, 4032 Debrecen, Hungary
[3]Department of Geology, Tanta University, 31527 Tanta, Egypt
[4]Petroleum & Mining Geology, Faculty of Science, Galala University, Egypt
[5]Fayoum University, Al-Fayoum, 63514 Egypt

DOI: 10.2581/zenodo.10254865

Abstract. The east of Gabal Atud area is covered by a variety of Precambrian basement rocks including Atud Formation, Atud tectonized mélange, metavolcanics, and serpentinites-talc-carbonates. These rocks were later intruded by the island arc metagabbro- diorite complex which in turn is invaded by some dykes. Operational Land Imager (OLI) and Sentinel-2A were applied for the first time for lithological discrimination of the exposed rock units in the east of Gabal Atud area. Five image enhancement techniques are applied including optimum index factor, false color composites, band rationing, principal component analysis, and minimum noise fraction for the interpretation of OLI and Sentinel-2A datasets. The integrated image-processing techniques allow the effective lithological discrimination of the east of Gabal Atud area, Central Eastern Desert, Egypt. The acid metavolcanics have been effectively discriminated from basic metavolcanics and serpentinites through FCC S2 b12-b11-b1, OLI PCA b4 -b3-b2, S2 PCA b5-b2-b3, and OLI band ratio (b4/b2, b6/b7, b4/b6). The sandstone facies highlight the fantastic (folding and faulting) structures of the Atud Formation on OLI and S2 images including OLI PCA of b1-b2-b3, S2 PCA of (b2), and S2 PCA of b5-b2-b3. Conglomerate facies can be differentiated from diamictite facies using the band ratio of the S2 (b7/b12). Although, the serpentinites and diamictite have different lithological compositions, they show similar colors in some OLI and S2 images (*e.g.* OLI PCA b1-b2-b3, S2 PCA b2) but they can be discriminated using other OLI and S2 techniques as OLI PCA b4-b2-b1, S2 PCA b5-b2-b3, and band ratio applications (*e.g.* OLI b6/b7 and OLI (b6/b7, b5/b6, b4/b2)).

Key words: Remote sensing, OLI, Sentinel-2A, Atud, Central Eastern Desert, Egypt

1. INTRODUCTION

The area east of Gabal Atud, the type locality of the Atud Formation, locates in the Central Eastern Desert of Egypt along Marsa Alam road (Fig. 1a) and covers an area of about 123 km^2 between latitude 24˚58´30˝N to 25˚03´00˝N and longitude 34˚25´30˝E to 34˚ 31´30˝E. The study area (Fig. 1b) is mainly covered by Atud Formation, metasediments (schist-mudstone-greywacke series, serpentinites-talc-carbonates, metagabbro-diorite complex, and grey granite (Essawy, 1964). The Atud Formation extends about 7.5 km E-W, and about 2-3 km wide and thrusted southward over the schist- mudstone-greywacke series and the serpentinites due to the emplacement of the massive Mubarak-Dabr metagabbro complex (Akaad and Essawy, 1964).

The tectonic setting, origin and depositional duration of the Atud Formation are still uncertain. The Atud conglomerates are considered to be deposited as part of an accreted prism due to the subduction of an oceanic plate in front of magmatic arcs (Soliman and Hegazy, 1989). The Atud conglomerates were suggested to be deposited in a continental environment rather than a deep-marine environment (Abu El-Ela, 1990).

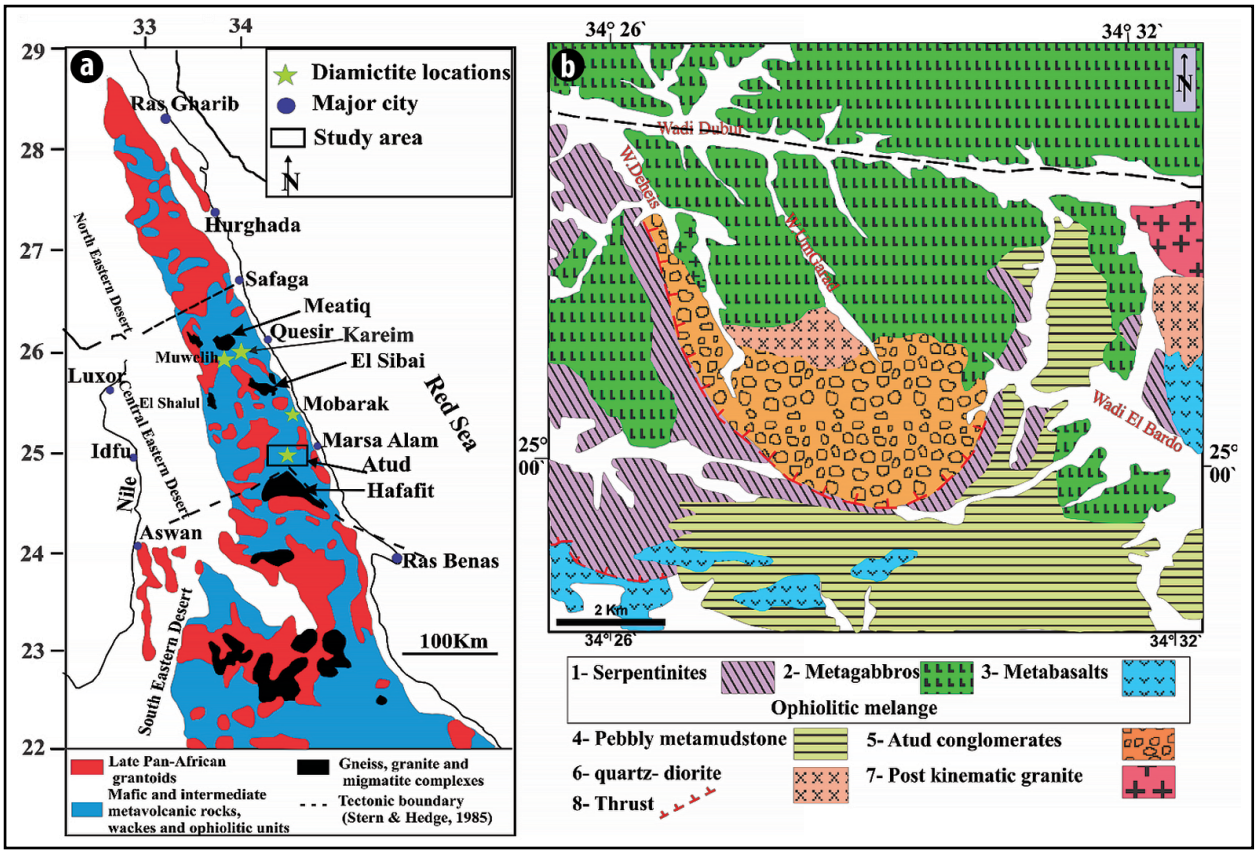

Fig. 1. (**a**) Geological map of the Eastern Desert of Egypt showing granitoids, gneisses, and arc units, along with basement subdivisions of North, Central, and South Eastern Dessert (modified after Ali *et al.,* 2015) Location of the study area is marked by the black rectangle. (**b**) Geological map of east Gabal Atud area (after Akaad and Essawy, 1965a; modified by Abu El Ela, 1990).

More recently, the Atud Formation was assumed to be deposited between 720 and 700 Ma, concurrent with the production of oceanic arcs in the Arabian Nubian Shield (ANS), but before the collision of the juvenile arc terranes with the continental crust (Li *et al.,* 2018).

The metagabbro represents the southern part of the extensive masses of Wadi Dabr metagabbro exposed within the Precambrian basement complex in the Eastern Desert of Egypt. These metagabbro rocks were named epidiorite (Amin *et al.,* 1953), epidiorite–diorite association (El-Ramly and Akaad, 1960), and metagabbro–diorite complex (Akaad and Essay,1964b). The rocks constituting the complex extended N-S about 40km, from Wadi Mubarak to Gabal Atud and about 34km E-W, from Gabal Igla El- Ahmar to Gabal Homret Waggat (Essawy, 1976). The Atud metagabbro consists of metagabbro, metadiorite, and metabasalt, together with minor relics of the original gabbros and hybrid diorites with appinitic tendencies. More recently, U–Pb zircon age determinations were carried out for the gabbroic and dioritic rocks from the Atud igneous complex in the Eastern Desert (Stern *et al.,* 2020), the results show that the rocks are the same age (U–Pb zircon ages of 694.5 ± 2.1 Ma for two diorites and 695.3 ± 3.4 Ma for one gabbronorite) and the Atud magmas formed above a subduction zone as part of a large and long-lived (c. 60 myr) convergent margin.

Remote sensing data have proven their eligibility in various geological applications, particularly in lithological mapping (Sadek *et al.,* 2015; Dawoud *et al.,* 2017; Shebl *et al.,* 2021; Abdelkader *et al.,* 2022; Dawoud *et al.,* 2022), detection of structural features (Abd El-Wahed *et al.,* 2019; Shebl and Csámer, 2021a, 2021b; Badawi *et al.,* 2022) and targeting mineral deposits in arid and semi-arid areas (El-Desoky *et al.,* 2022; El-Magd *et al.,* 2015; Shebl and Csámer, 2021b).

The lithological discrimination based on remote sensing data mainly depends on the differences in physical and chemical properties between all rock types, mineralogy, weathering characteristics, elevation, and vegetation distribution (Xiong *et al.,* 2011). Moreover, the spectral characteristics and textural features of the rocks in satellite images are influenced by tectonics, weathering, drainage or erosion. Comprehensive data on the mineralogy of various rock types on the Earth's surface were provided due to the advancement of remote sensing technology (*e.g.* Zhang *et al.,* 2007), many image processing techniques have been developed to map the boundaries of rock bodies, weathered rock zones, and hydrothermally altered rock zones, particularly in arid regions with no or little vegetation cover (*e.g.* Loughlin, 1991; Abdelsalam and Stern 2000; Ramadan *et al.,* 2001; Kusky and Ramadan 2002; Liu *et al.,* 2007; Gaber

et al., 2015; Ali-Bik *et al.,* 2012; Zoheir and Emam 2012; Sadek *et al.,* 2015; Dawoud *et al.,* 2017; Emam *et al.,* 2018; Shebl *et al.,* 2021; Shebl and Csámer, 2021a; Dawoud *et al.,* 2022; Abdelkader *et al.,* 2022).

This study aims to produce for the first time a novel detailed geological map for the east of Gabal Atud area based on the analysis of remote sensing data, earlier geological mapping, field validation, and petrographic studies using the integrated data of S2-A and Landsat-8 satellite images, to improve lithological discrimination of various rock types in the east of the Gabal Atud area.

2. MATERIALS AND METHODS

2.1. Remote sensing data

Two multispectral datasets, including Operational Land Imager (OLI) and Sentinel-2A (S2) were downloaded from the USGS website (https://earthexplorer.usgs.gov) and used in this study. The Landsat-8 satellite, launched in February 2013, carries the OLI and Thermal Infrared Sensor (TIRS) that senses the Earth's land surface with a 16-day repeat cycle over a 185 km wide swath (Irons *et al.,* 2012; Loveland and Irons, 2016). Landsat OLI provides images of nine spectral wavelengths with a spatial resolution of 30 meters for VNIR (Table 1). Sentinel-2 satellites are operated by the European Space Agency (ESA) and are equipped with a Multi-Spectral Instrument (MSI) to image the ground at an altitude of nearly 786 km (Drusch *et al.,* 2012). Sentinel-2 MSI data comprises 13 spectral bands (Table 1) with a spatial resolution ranging from 10 to 60 m (Drusch *et al.,* 2012; Shebl *et al.,* 2021; Abdelkader *et al.,* 2022). Due to their spatial and spectral variability among the OLI and S2, their integrated results could generate more detailed lithological discrimination for the study area.

2.2. Data Pre-processing

The cloud-free Landsat 8 (Granule ID: "LC817404320 17100LGN00") and Sentinel-2A (Granule ID "L1C_T36RXN_ A036826_20220711T081249") scenes are atmospherically corrected and resized. The Landsat 8 OLI images are resampled to 15 m spatial resolution, atmospherically corrected, and layer stacked using image processing and analysis software version (ENVI V5.3.). Sentinel-2A cloud-free images are resampled to 10 m spatial resolution, and layer stacked into one file using the ESA-provided Sentinel Application Platform (SNAP) software.

2.3. Methods

OLI and S2 data are processed using several techniques such as Optimum Index Factor (OIF), False Color Composite (FCC), Principal Component Analysis (PCA), Minimum Noise Fraction (MNF), and Band Rationing (BR). These techniques are integrated to re-map the rock units of the east of Gabal Atud area, according to our adopted workflow (Fig. 2). The resultant grayscale and false-colored images have been interpreted to obtain information about the rock units exposed in the study area.

2.3.1. Optimum index factor (OIF)

The Optimum Index Factor is a statistical value that is often used to designate the best three-band combinations out of all possible three-band combinations to create a color composite (Chavez *et al.,* 1982; Chavez, 1984, Shebl and Csámer, 2021a; Abdelkader *et al.,* 2022).

Table 1. Characteristics of landsat 8 and Sentinel- 2A MSI data (Barsi *et al*., 2014; Drusch *et al*., 2012)

Landsat- 8 (OLI)				Sentinel 2A			
Bands	**Spectral Region**	**Central Wavelength (µm)**	**Spatial Resolutions**	**Bands**	**Spectral Region**	**Wavelength (µm)**	**Spatial Resolutions**
1	Coastal aerosol	0.433 - 0.450	30m	**1**	Ultra Blue	0.433 - 0.453	60m
2	Blue	0.450 - 0.515	30m	**2**	Blue	0.458 - 0.523	10m
3	Green	0.525 - 0.600	30m	**3**	Green	0.543 - 0.578	10m
4	Red	0.630 - 0.680	30m	**4**	Red	0.650 - 0.680	10m
5	VNIR	0.845 - 0.885	30m	**5**	VNIR	0.698 - 0.713	20m
6	SWIR	1.560 - 1.660	30m	**6**	VNIR	0.733 - 0.748	20m
7	SWIR	2.100 - 2.300	30m	**7**	VNIR	0.773 - 0.793	20m
8	Panchromatic	0.500 - 0.680	15m	**8**	VNIR	0.785 - 0.899	10m
9	Cirrus	1.360 - 1.390	30m	**8A**	VNIR narrow	0.855 - 0.875	20m
				9	SWIR water vapor	0.935 - 0.955	60m
				10	SWIR cirrus	1.360 - 1.390	60m
				11	SWIR	1.565 - 1.655	20m
				12	SWIR	2.100 - 2.280	20m

VNIR = visible near-infrared, **SWIR** = short wave infrared, and **TIR** = thermal infrared

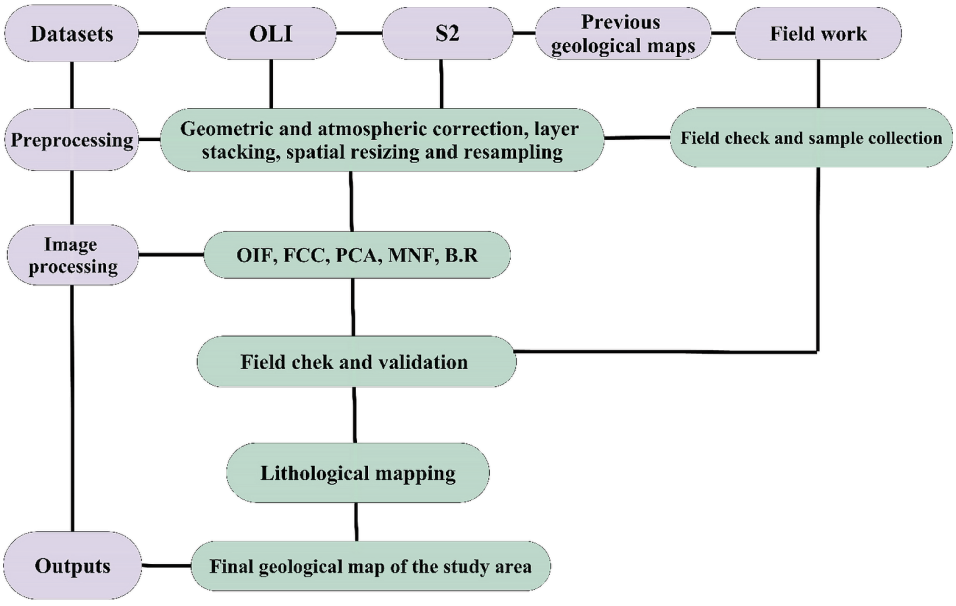

Fig. 2. Flow chart for lithologic mapping of east of Gabal Atud area based on the integrated OLI data and Sentinel-2A.

ILWIS software version 3.8. was applied to compute the OIF to find the suitable band combination with the least redundancy and highest feature identification. ILWIS open software applies the following algorithm to obtain the highest-ranked OIF index, based on equation (1) (Chavez, 1984):

$$OIF = \frac{Si + Sj + Sk}{|Ri,j| + |Ri,k| + |Rj,k|} \quad (1),$$

where Si, Sj, and Sk are the standard deviation for bands I, j and k respectively, and Ri,j, Ri,k, and Rj,k are the correlation coefficients between any two of the three bands being evaluated.

2.3.2. False-color composite (FCC)

False-color composites are the representation of any three bands in an order that differs from True Color Composite (TCC). Many different false-colored composites are applied to highlight different lithological features and hydrothermal alteration zones in the Eastern Desert (*e.g.* Emam *et al.,* 2018; Abd El- Wahed *et al.,* 2019 Dawoud *et al.,* 2022; Abdelkader *et al.,* 2022).

2.3.3. Principal component analysis (PCA)

Principal component analysis is a mathematical algorithm used to analyze the correlated multispectral datasets that are arranged along with the greatest variability axis to produce new non-correlated components (Pearson, 1901; Crosta *et al.,* 2003; Ranjbar *et al.,* 2004; Richards, 2012). Simply, this transformation technique analyses and removes the redundancy of information that occurs between the dissimilar bands to extract valuable information from them (Loughlin, 1991; Gomez *et al.,* 2005; Gasmi *et al.,* 2016) and is usually employed to construct powerful color composites, which improves the visual perception of surface material mapping (Yamaguchi and Naito, 2003; Shebl *et al.,* 2021; Abdelkader *et al.,* 2022).

2.3.4. Minimum noise fraction (MNF)

The Minimum noise fraction transformation technique applies to equalize noise in imaging data and reduce the computations required for successive image processing (Green *et al.,* 1988; Pournamdari *et al.,* 2014). The minimum noise fraction (MNF) approach is an orthogonal rotation that can generate components organized in increasing rank of random noise rather than decreasing rank of variance in principal components (Kruse *et al.,* 2003; Khan *et al.,* 2007; Liu *et al.,* 2009; Berman *et al.,* 2012; Lixin *et al.,* 2015; Assiri, 2016).

2.3.5. Band rationing (BR)

Band rationing is a mathematical transformation technique based on the division of one spectral band by another (Sabine, 1999; Sabins and Floyd, 1986). It allows the investigation of the absorption features of objects and leads to more enhanced gray-scale images compared with the original data (Drury, 2001). In geological applications, BR is considered a simple and effective method for decreasing the effect of topography and increasing the minor differences in spectral reflectance properties of rocks and soils (Rowan *et al.,* 2003; van der Meer *et al.,* 2012; Langford, 2015; Corumluoglu *et al.,* 2015). Additionally, it may emphasize specific features or materials that cannot be highlighted in the individual raw band (Sabine, 1999; Ninomiya 2003; Mars and Rowan, 2006).

2.4. Validation: Field and petrographic investigation

The resultant information from the processed remote sensing data has been confirmed by fieldwork as the lithological boundaries of the basement rocks exposed in the

study area have been identified as well their field relations have been verified. Representative samples from different rock units were collected, and petrographic studies were operated to validate the resultant remote sensing data.

3. RESULTS AND DISCUSSION

The OLI and Sentinel-2A data were applied for the first time in the east of Gabal Atud area, resulting in comprehensive lithological discrimination and geological mapping of the exposed lithologies. Remote sensing results were integrated with field investigations, preceding geological maps (*e.g.* Essawy 1964; Akaad and Essawy 1964; Abu El-Ela, 1990) as well as the petrographic studies to construct a novel detailed geological map for the east of Gabal Atud area.

3.1. Remote sensing results

3.1.1. Optimum index factor (OIF)

Applying the OIF algorithm for seven OLI-reflected VNIR- SWIR bands results in six color combinations ranked according to the highest OIF values in (Table 2). So, the best color composites for lithological mapping within the study area include composite bands of b7-b6-b1 in RGB. These band combinations are the most informative images to discriminate between the rock units, in addition, highlight the main structural features in the study area. The RGB color composite of b7-b6-b1 enhances basic metavolcanics (Mvb) with blue, from the acid metavolcanics (Mva) with yellow-green color (Fig. 3a). Serpentinites (Srp), and diamictite (Dm) show similar colors, and metagabbro (Mgb) exhibits brown color.

3.1.2. False-color composite (FCC)

OLI and S2 FCC images mainly give precise information about the exposed basement rocks and the lithological boundaries for the geological map. According to the OLI FCC of b7-b5-b1 (Fig. 3b), the metagabbro show deep violet color at the north of the study area, toward the south at the contact with the Atud Formation, a belt of the metagabbro exhibits a light color and different texture, this may be attributed to the differentiation of the metagabbro into diorite, and/ or the intrusion of the metagabbro into the Atud Formation as it encloses xenoliths of diamictite (greenish blue).

Applying S2 FCC of b12-b11-b1 produces an image with high resolution (Fig. 3c) effectively used in mapping serpentinites (Srp), basic metavolcanics (Mvb) and diamictite (Dm) in blue, metagabbro (Mgb) with brown color, the acid metavolcanics (Mva) with green color, conglomerates (Cgl) with dark olive green and sandstone (Ss) with buff color. S2 FCC b12-b6-b2 (Fig. 3d), differentiates the basic metavolcanics (Mvb) and serpentinites (Srp) in greenish-blue color, the acid metavolcanics (Mva) in light brown, the Atud Formation as greenish-blue, olive green and red color for diamictite (Dm) facies, conglomerates (Cgl) facies and sandstone (Ss) facies, respectively.

3.1.3. Principal component analysis (PCA)

The PCA transformation technique is computed for OLI VNIR- SWIR and S2 bands to obtain the best informative PCA color composite. The obtained data reveal that the OLI PCA b2 grey-scale image (Fig. 4a) and S2 PCA b2 grey-scale image (Fig. 4b) are the best for mapping the sandstone facies, as well as to differentiate the serpentinite and the basic metavolcanics with a bright tone from acid metavolcanics with a dark tone. As the S2 PCA b2 shows the highest resolution, it enhances the faulting and folding structures affecting the Atud Formation that are mostly indicated by repeated, folded and faulted strips of the sandstone (Ss) facies with dark tones alternated with the diamictite facies with grey tones.

The OLI color combination of PCA b1-b2-b3 in RGB (Fig. 4c) differentiates the sandstone facies in maroon and red color, the color of the sandstone becomes lighter southward with increasing the portion of the intercalations with the conglomerate toward the southeast of the Atud Formation. The metagabbro appears cyan and its color changes to purple at the contact with the sandstone facies of the Atud Formation. Serpentinites, basic metavolcanics and diamictite display similar colors (sky blue).

On the other hand, the OLI PCA of b4-b2-b1 in RGB image (Fig. 4d) discriminates serpentinites and basic metavolcanics with bright green from the conglomerates and diamictite facies of the Atud Formation which displays dark yellow and bright-yellow colors, respectively. Moreover, the OLI PCA b4-b3-b2 in RGB (Fig. 5a), discriminates serpentinites and basic metavolcanics with aqua blue color from the diamictite with white color, and conglomerate with pinkish white. It also enhances the acid metavolcanics with yellowish- green color.

Table 2. OIF Index highest ranking of OLI VNIR- SWIR bands

N	Red	Green	Blue	Rank %
1	Band 6	Band 2	Band 1	70.54
2	Band 7	Band 2	Band 1	70.46
3	Band 7	Band 6	Band 1	70.25
4	Band 7	Band 3	Band 1	69.30
5	Band 7	Band 6	Band 2	69.17
6	Band 6	Band 3	Band 1	69.11

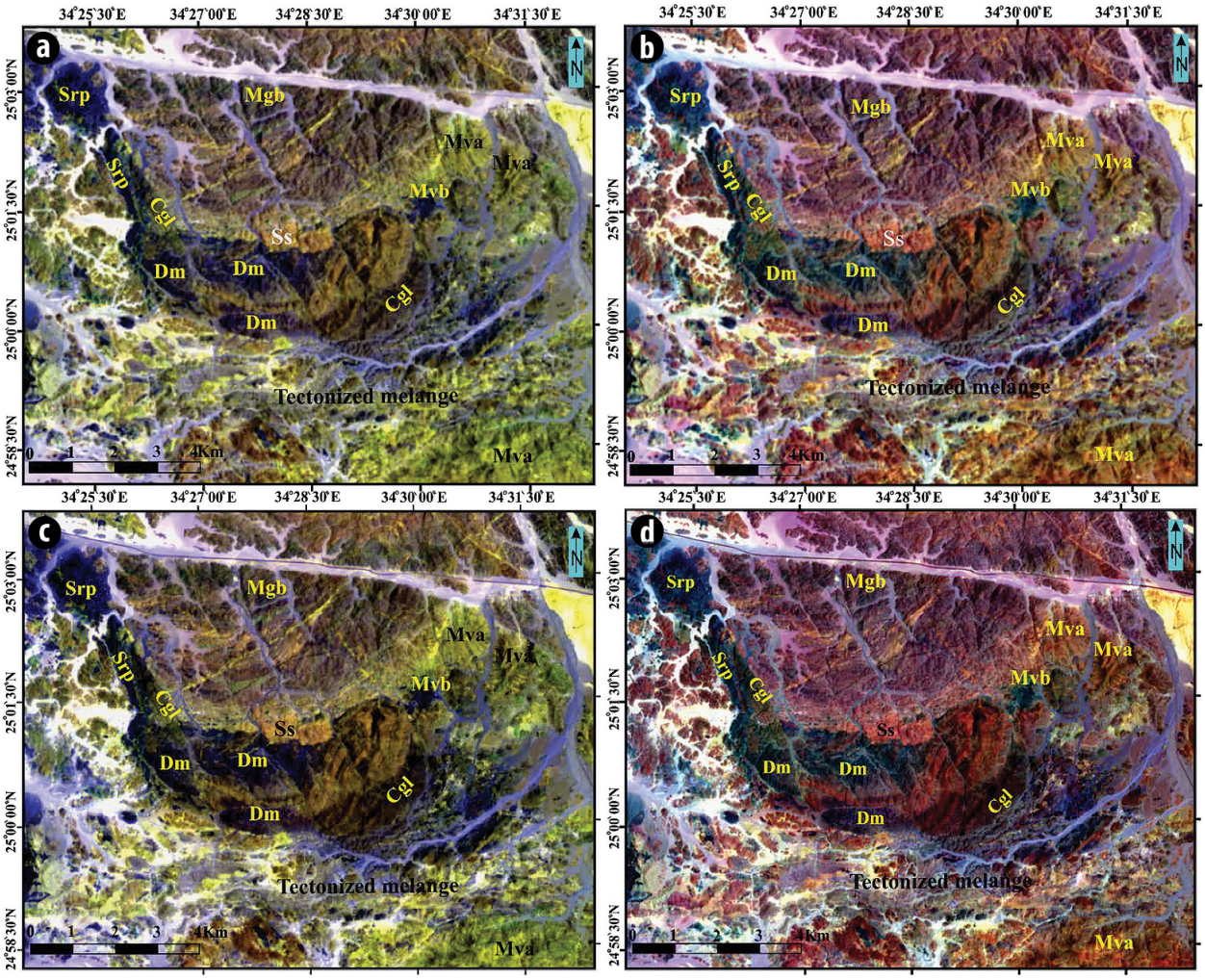

Fig. 3. FCC of OLI and S2. (**a**) FCC OLI OIF image of b7-b6-b1 as RGB of OIF rank 3; (**b**) FCC OLI b7-b5-b1 as RGB; (**c**) FCC S2 b12-b11-b1 as RGB; (**d**) FCC S2 b12-b6-b2 as RGB. Serpentinite (Srp), basic metavolcanics (Mvb), Acidic metavolcanic (Mva), metagabbro (Mgb), diamictite (Dm), conglomerate (Cgl), sandstones (Ss).

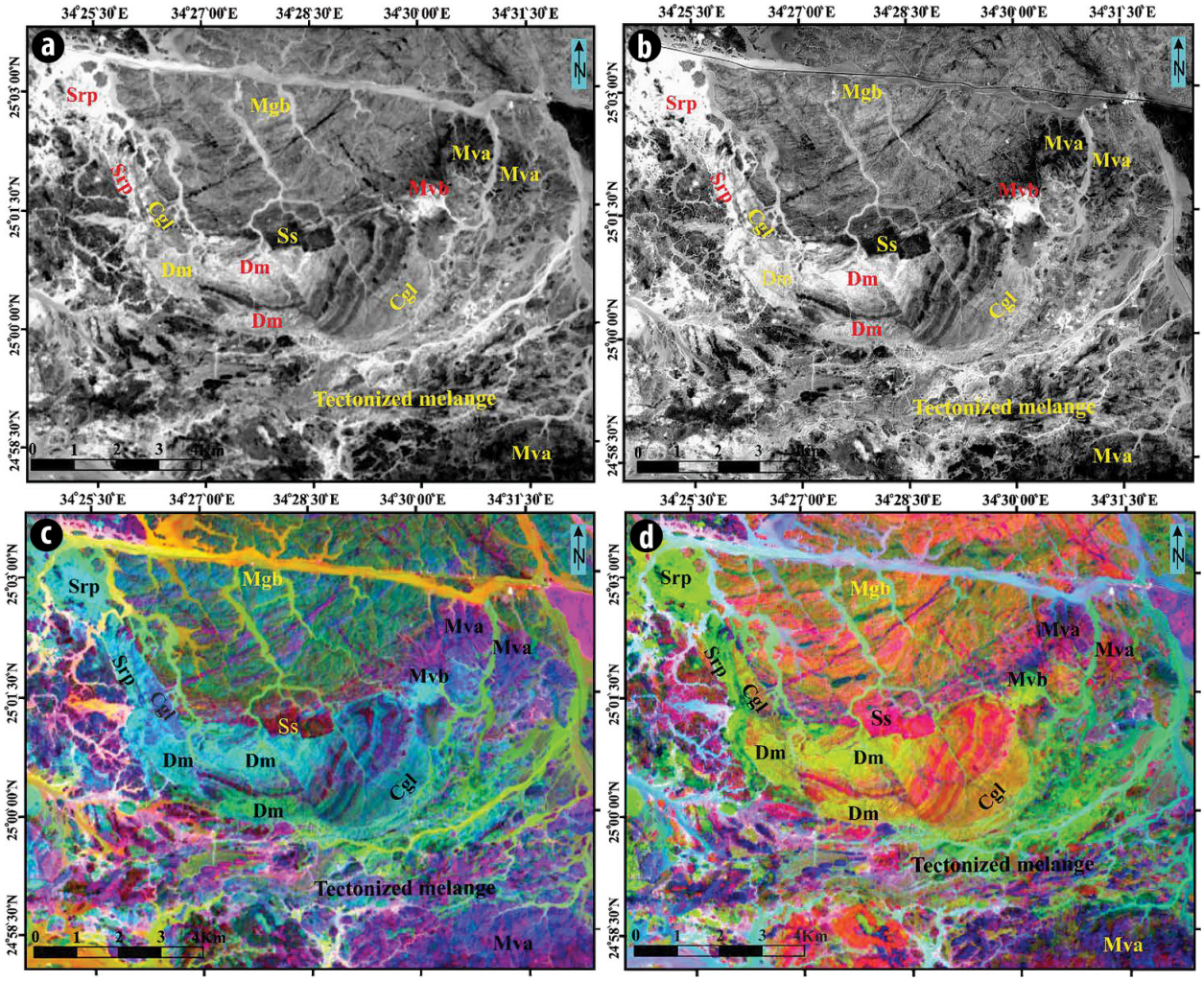

Fig. 4. PCA resultant images of OLI and S2 (VNIR-SWIR) bands east of Gabal Atud area. (**a**) OLI PCA of (b2) grey-scale image; (**b**) S2 PCA of (b2) grey-scale image; (**c**) OLI PCA b1-b2-b3 in RGB; (**d**) OLI PCA b4-b2-b1 in RGB.

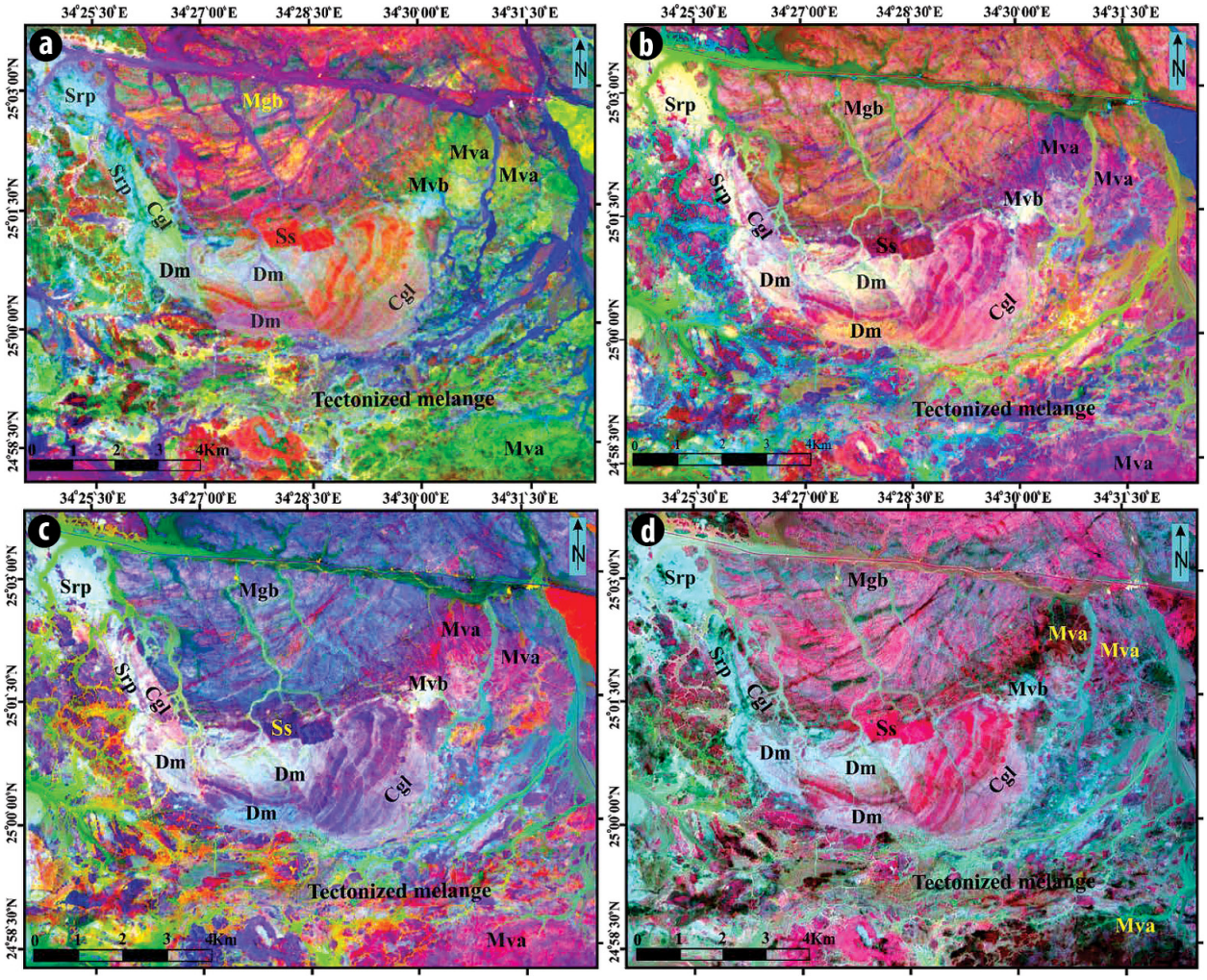

Fig. 5. PCA results of OLI and S2. (**a**) OLI PCA b4 -b3-b2 in RGB; (**b**) S2 PCA b1-b2-b3 in RGB; (**c**) S2 PCA b3-b2-b1 in RGB; (**d**) S2 PCA b5-b2-b3 in RGB.

The S2 PCA b1-b2-b3 (Fig. 5b) and S2 PCA b3-b2-b1 (Fig. 5c) images help in the verification of the rock units and deducing the boundaries of rock units. The S2 PCA b3-b2-b1 differentiates metagabbro in blue, acid metavolcanics in purple, while serpentinites, basic metavolcanics, diamictite and conglomerates show similar whitish colors. Sandstone displays a violet color.

Otherwise, serpentinites and basic metavolcanics can be discriminated with bright blue color on the S2 PCA color combination of b5-b2-b3 (Fig. 5d), while the sandstone, conglomerate and diamictite facies of the Atud Formation display pink, pinkish white and bright white colors, respectively. The acid metavolcanics show reddish brown color, while the metagabbro shows a variation of colors.

3.1.4. Minimum noise fraction (MNF)

As a well-known technique for delivering potential lithological discrimination, the OLI MNF2 grey-scale image reveals the serpentinites and the basic metavolcanics in a dark tone while the acid metavolcanics display a bright tone (Fig. 6a). The S2 MNF4 grey-scale image is more effective in the discrimination of serpentinites and basic metavolcanics with a black tone (Fig. 6b). Diamictite, conglomerate and acid metavolcanics display grey tones. Metagabbro shows pale grey tones while sandstone shows bright tones.

The processed color composite image of OLI data of MNF1-MNF2-MNF3 discriminates the lithology and the structure affecting the study area, especially the Atud Formation. The OLI color combination of the MNF1-MNF2-MNF3 image (Fig. 6c) discriminates the serpentinites and basic metavolcanics with pink, metagabbro with purple and sandstone with blue.

The Sentinel-2A band combination of MNF5-MNF4-MNF3 in RGB (Fig. 6d) differentiates the serpentinites and basic metavolcanics with blood red color, diamictite with light red color, conglomerates with bronze color, and sandstone (Ss) with yellow color. The acid metavolcanic shows a sky blue color while the metagabbro shows varied colors.

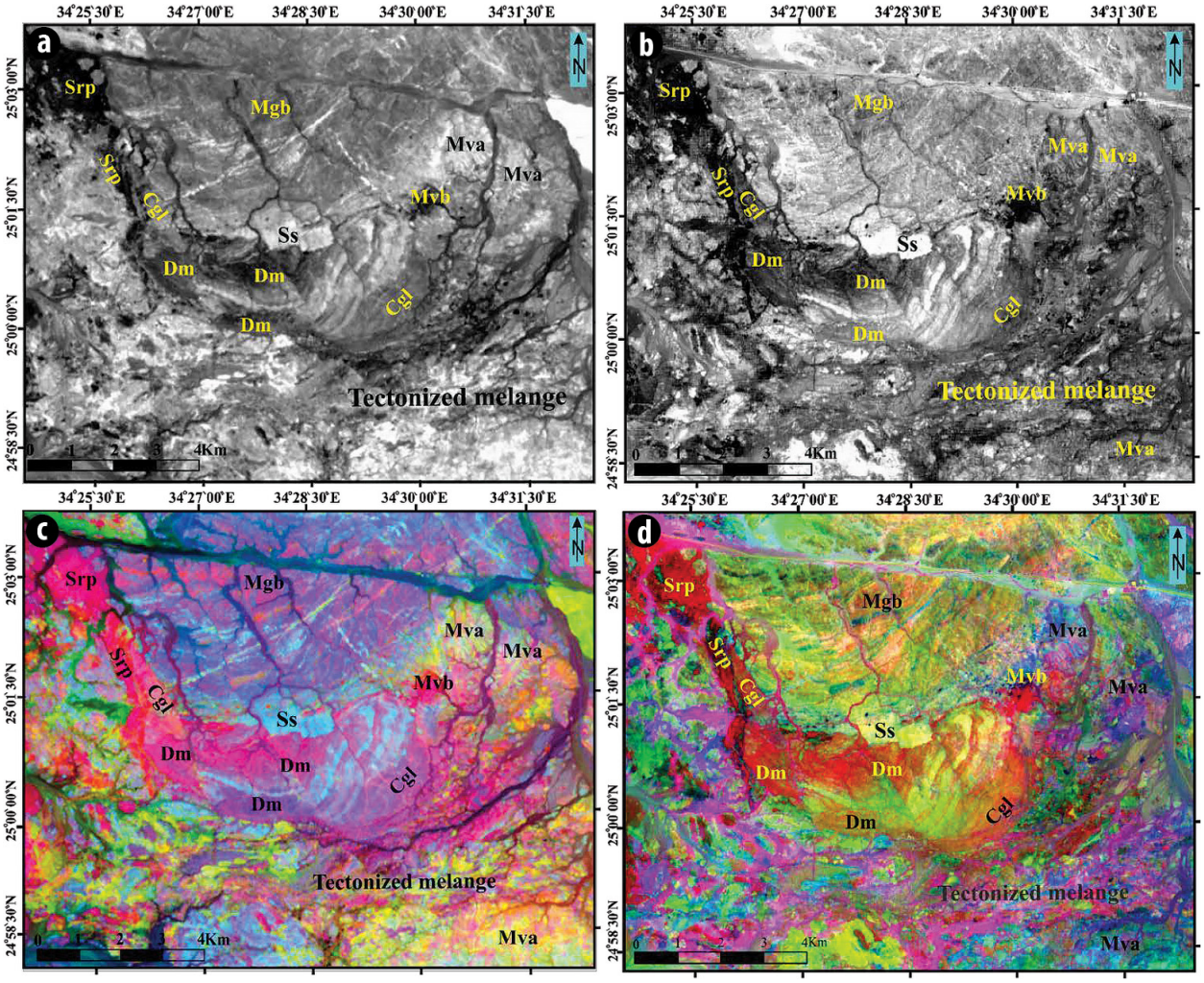

Fig. 6. MNF resultant images of OLI and S2 (VNIR- SWIR) bands. (**a**) OLI MNF2 grey- scale image; (**b**) S2 MNF4 grey-scale image; (**c**) OLI MNF1-MNF2-MNF3 in RGB; (**d**) S2 MNF5-MNF4-MNF3 in RGB.

3.1.5. Band rationing (BR)

The band rationing results are extremely useful for structure delineation and detailed lithological mapping of the east Atud area. The OLI band ratios (b6/b7, b7/b3, b6/b2, b6/b5, b4/b2, b5/b6, b4/b5, b7/b3) were processed to discriminate the different rock units exposed in the study area. The band ratio (b6/b7) is the best to discriminate the serpentinites and the basic metavolcanics in a bright tone (Fig. 7a) due to the band 7 absorption features by MgO– and OH–bearing minerals around OLI band 7 (2.1–2.3 µm) and reflectance features around OLI band 6 (1.56–1.66 µm) (Sultan *et al.,* 1986; Gad and Kusky, 2006; Emam *et al.,* 2018). On the other, the OLI band ratio (b7/b3) brings out the serpentinites and the basic metavolcanics with dark tones, diamictite, conglomerates, and metagabbro show grey tones, while the sandstone and the acid metavolcanics have bright tones as shown in (Fig. 7b).

Additionally, the OLI (b5/ b6) image (Fig. 7c), and S2 (b7/b12) band ratio are both informative for the lithological differentiation of the exposed rock units. S2 (b7/b12) is a high-resolution image that brings out the serpentinites and the basic metavolcanics with a bright tone, the diamictite with light grey, the conglomerate with a grey tone, the sandstone with a dark tone, and acid metavolcanics with a black tone (Fig. 7d).

The OLI band ratio (b6/b7, b5/b6, b4/b2) distinguishes, after (Abrams *et al.,* 1983), the serpentinites and basic metavolcanics with yellow color. The diamictites and conglomerates of the Atud Formation have a green color, while the sandstone facies show blue color and the acid metavolcanics show purple color (Fig. 8a).

The OLI band ratios (b4/b2, b6/b7, b4/b6) discriminate the serpentinites and the basic metavolcanics with bright blue color (Fig. 8b) and diamictites with sky blue color. The serpentinites and the basic metavolcanics display white color, the diamictites and the conglomerates have a yellow color, sandstones show dark green color, while the acid metavolcanics have blue color according to OLI band ratios (b4/b6, b5/b6, b6/b7) (Fig. 8c).

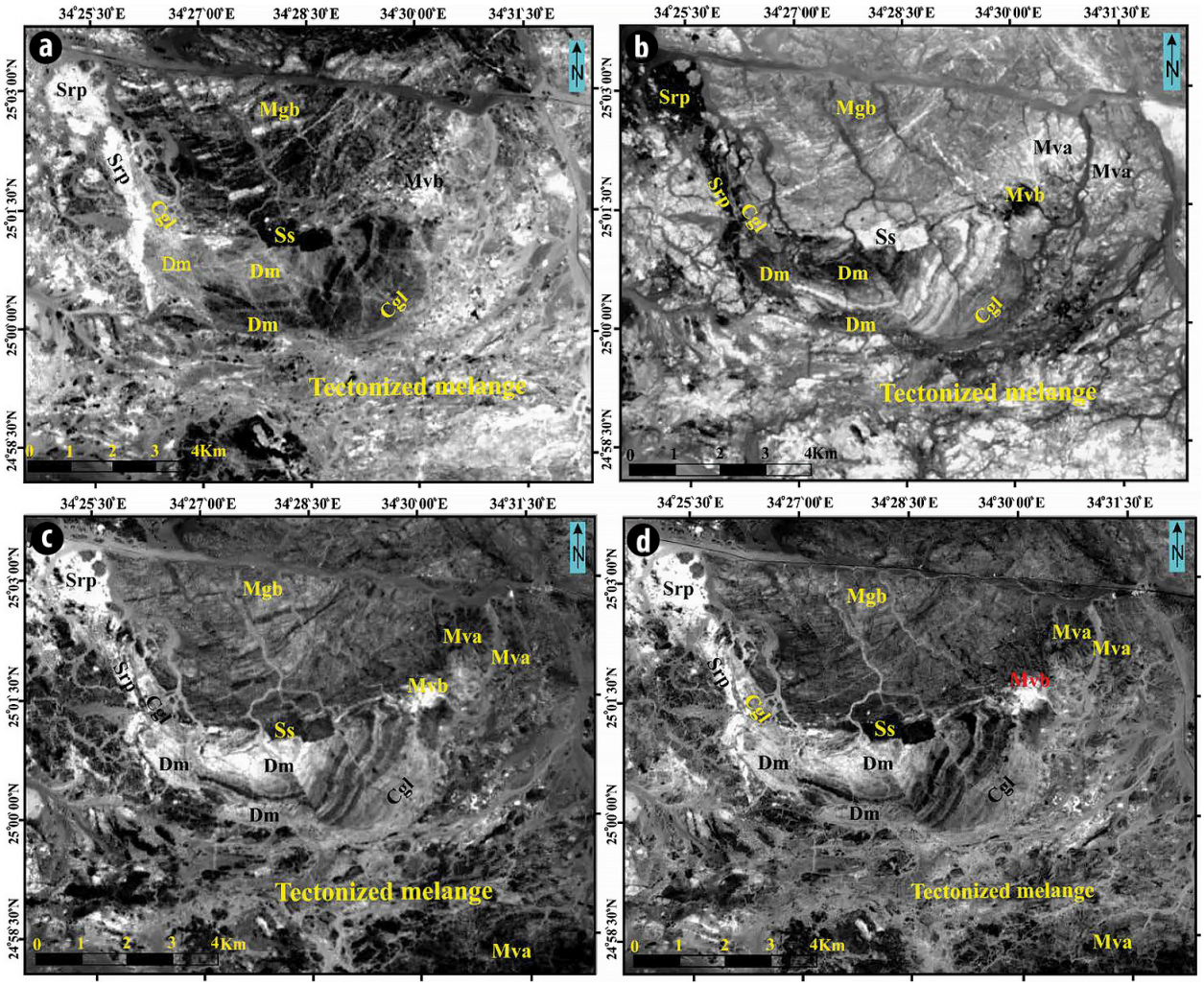

Fig. 7. Band ratio images of S2 and OLI data of the study area. (**a**) OLI (b6/b7); (**b**) OLI (b5/b6); (**c**) OLI (b7/b3); (**d**) S2 (b7/b12).

Also, the use of OLI band ratios (b6/b7, b7/b3, b6/b5) image effectively discriminates the serpentinites and the basic metavolcanics (light red) from the diamictites (dark red) (Fig. 8d).

4. GEOLOGY AND GEOLOGICAL SETTING

The geology and geological setting of the area east of Gabal Atud are executed from the remote sensing data which in turn are confirmed by the field and the petrographic studies resulting in a new detailed geological map (Fig. 9) for the east of Gabal Atud area. The field relations revealed that the basement stratigraphic sequences exposed in the area east of Gabal Atud are sometimes overlapped and synchronized rather than reflecting subsequent geological processes.

The basement rocks of the study area are classified into Atud Formation, Atud tectonized mélange, metavolcanics, serpentinites-talc-carbonate, and the metagabbro-diorite rocks, in addition to some dykes, in decreasing age.

In the present study, the authors assume that the term diamictite is more proper to describe the poorly sorted, polymictic, chaotic and matrix-supported rocks constituting the Atud Formation (Flint *et al.,* 1960; Bates and Jackson, 1987; Eyles and Januszczak, 2004; Stern *et al.,* 2006). Furthermore, the term tectonized mélange is more suitable than the term 'Schist-metamudstone group' to describe the mélange that was only deposited by sedimentary depositional processes and not by tectonic ones, though it has been tectonically disturbed somewhat through its later history (Berkland *et al.,* 1972; Schuster, 1980; Erickson, 2011; Dilek *et al.,* 2012; Festa *et al.,* 2019).

4.1. Atud Formation

The Atud Formation outcrops as a curvilinear belt of about 10.5 km^2 exposed in the center of the study area surrounded northward by the metagabbro-diorite complex, west and southward by serpentinites and related rocks, and eastward by the Atud tectonized mélange and metavolcanics. The Atud Formation comprises three facies, namely diamictite, conglomerate and sandstone.

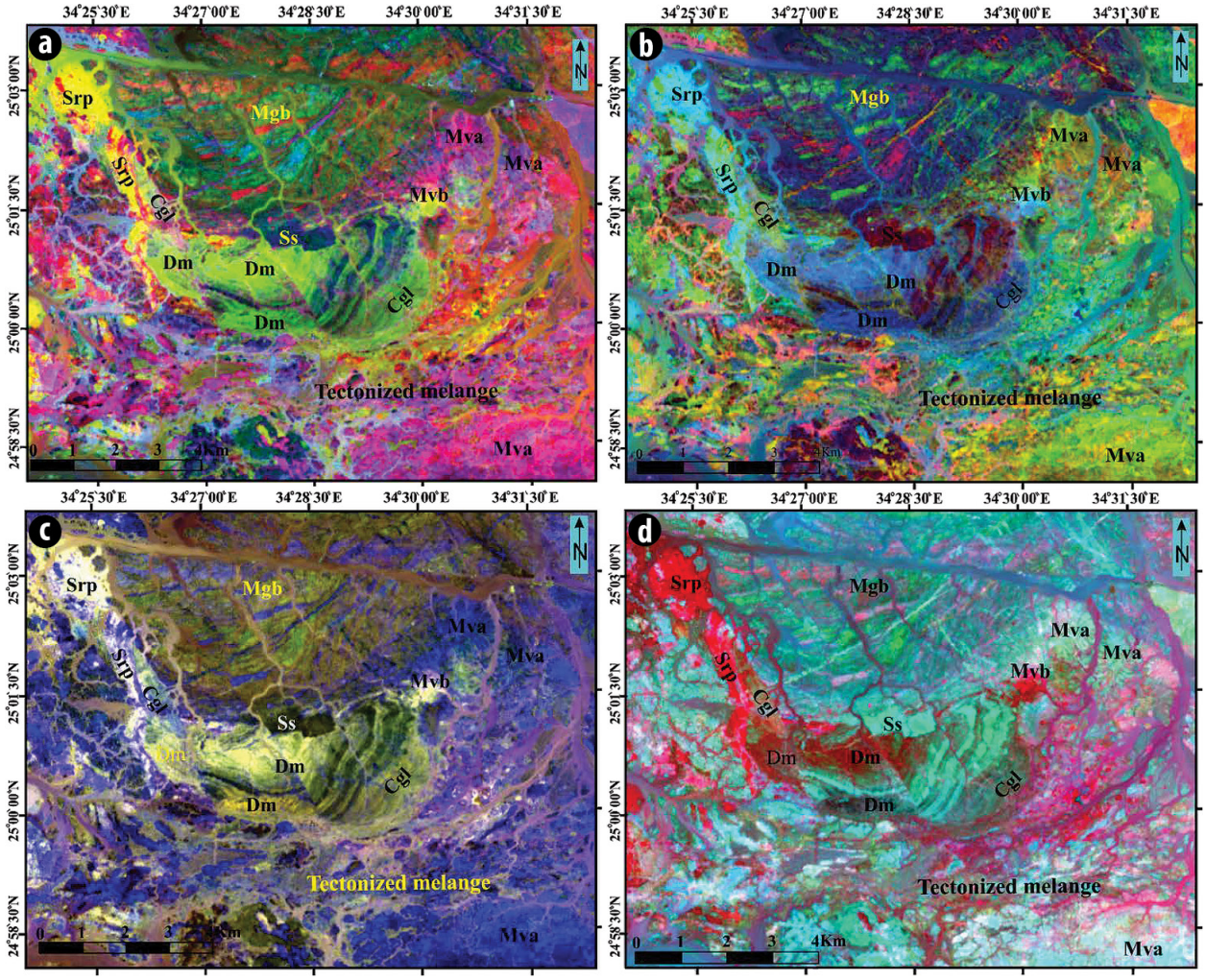

Fig. 8. Band ratio images of OLI data. (**a**) OLI band ratio (b6/b7, b 5/b6, b4/b2) in RGB; (**b**) OLI band ratio (b4/b2, b6/b7, b4/b6) in RGB; (**c**) OLI band ratio (b4/b6, b5/b6, b6/b7) in RGB; (**d**) OLI band ratio (b6/b7, b7/b3, b6b/5) in RGB.

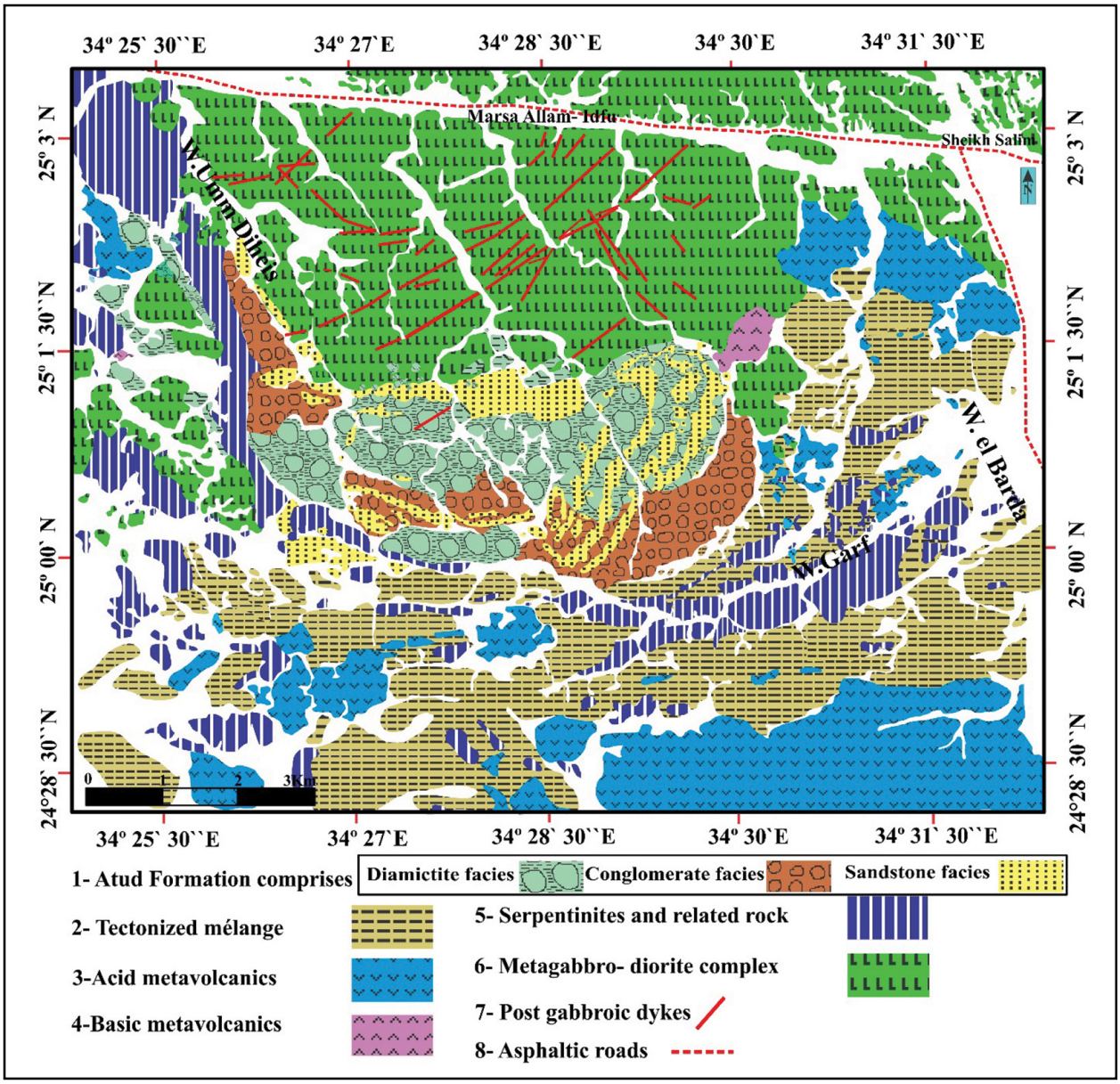

Fig. 9. New detailed geological map of east Gabal Atud area.

The three facies exhibit steeply tilted bedding and repetitive lateral alternations (Fig. 10a). The Atud Formation is characterized by the entire absence of serpentinites, gneisses and basic metavolcanic lithic fragments.

4.1.1. Diamictite lithofacies

Diamictite lithofacies is a term used to comprise and describe all the poorly sorted lithofacies exposed east of the Gabal Atud area which until that time were named matrix-supported conglomerates and pebbly metamudstones. The diamictite lithofacies are exposed in the core of the Atud Formation large fold and at its eastern periphery, displaying a polymict nature and occurring as chaotic, poorly sorted, grey and black colored rocks (Fig. 10b) devoid of bedding. The lithic fragments are rounded to subrounded, ovoidal to sphere-like shapes of variable sizes. Commonly, the lithic fragments are dominated by relatively unaltered acid volcanics (metarhyolite-porphyry), granitic rocks, carbonates (Fig. 10c,d,e), polycrystalline quartz, chert, reworked clastic sediments (greywacke and mudrock). The matrix bounding these lithic fragments is represented by pebbly mudrock and consists of a mixture ranging from pebble-sized lithic fragments and sand-sized grains to fine grains (Fig. 10f).

4.1.2. Conglomerate lithofacies

The conglomerate lithofacies is exposed in the northwest and southeast part of the Atud Formation. Both coarse and fine conglomerates are exposed and some conglomerates' exposures show a preferred alignment of the enclosed clasts along their long axes (Fig. 11a).

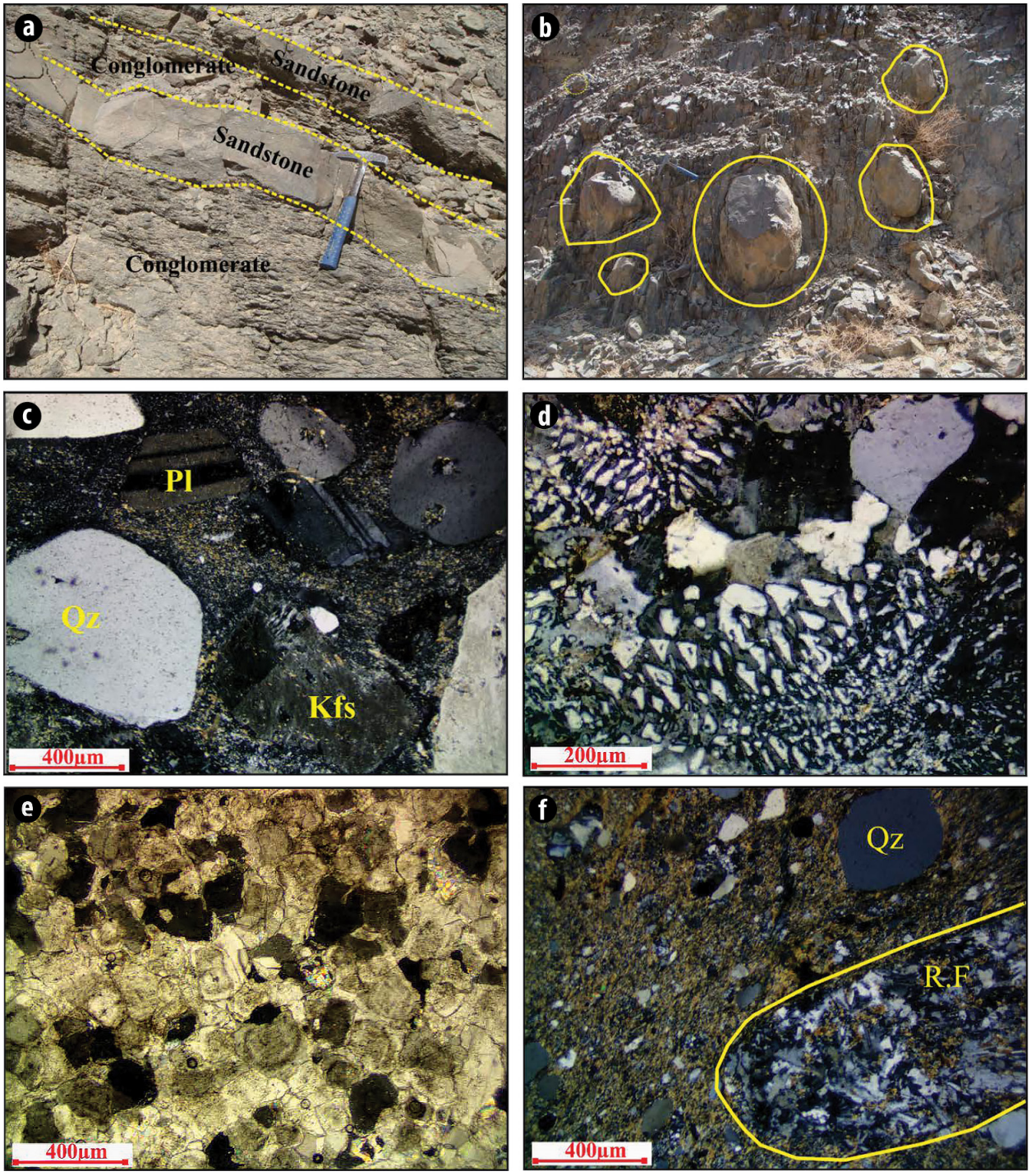

Fig. 10. (**a**) Field photograph shows alternative beds of sandstone (less eroded with blocky structure) and conglomerate with rough surface, Atud Formation; (**b**) Photograph showing rounded to subrounded granite and carbonate lithic fragments within diamictite facies; (**c**) Photomicrograph showing metarhyolite lithic fragments, Atud diamictite facies; (**d**) Photomicrograph showing the mineral composition [quartz (Qz), K-feldspar (Kfs), and plagioclase (Pl) and graphic texture of graphic granite lithic fragments, Atud diamictite facies; (**e**) Photomicrograph showing well crystalline zoned dolomite crystals in carbonate lithic fragment, diamictite facies; (**f**) Photomicrograph showing rock fragment (R.F) embedded in sandy mud matrix of the diamictite.

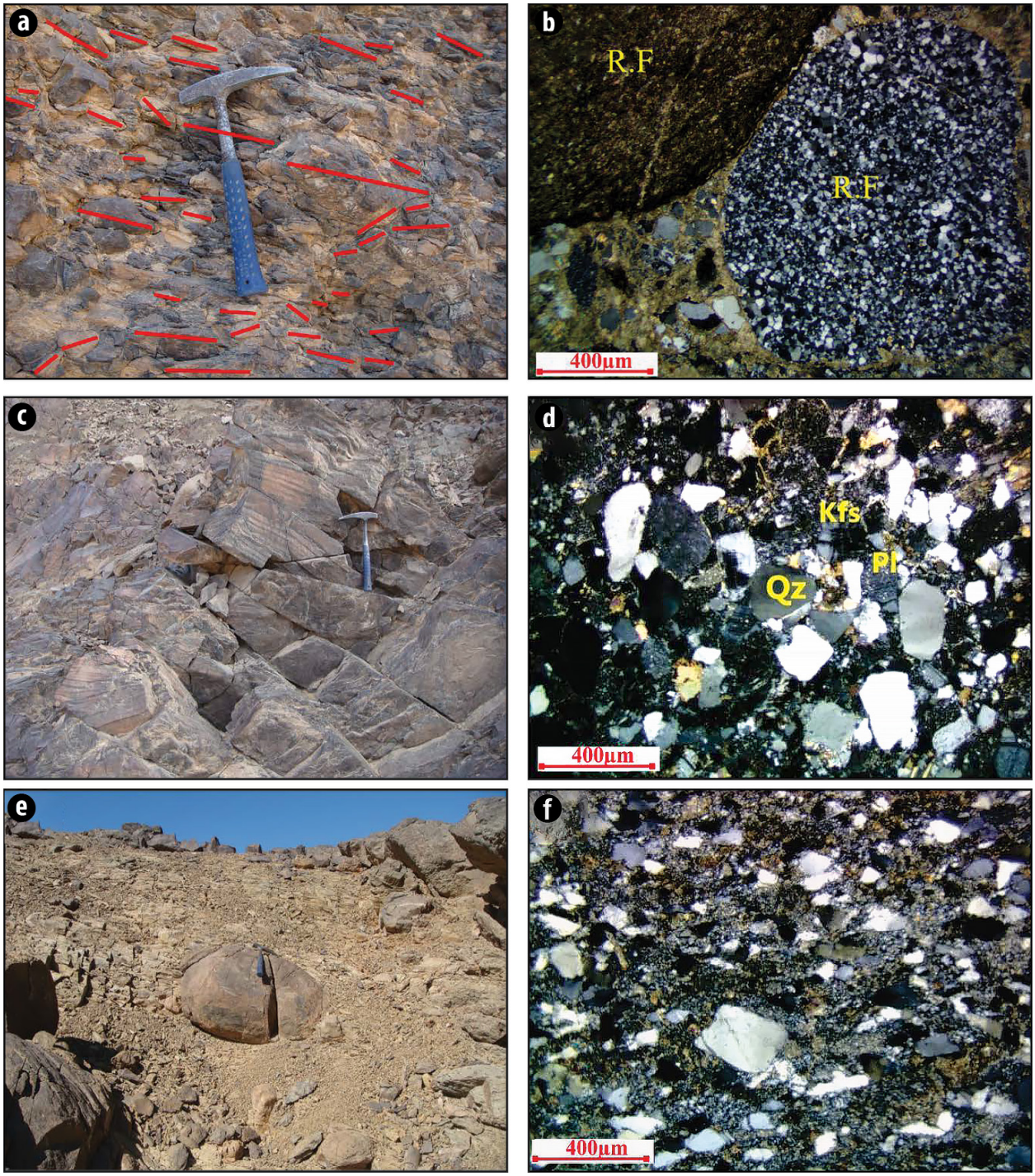

Fig. 11. (**a**) Photograph showing parallel to sub-parallel aligned rock fragments in grain-supported conglomerate facies; (**b**) Photomicrograph showing chert microclasts and reworked sediments within mud-carbonate-quartz matrix, conglomerate facies; (**c**) Photograph showing erosional-related banding in sandstone facies due to variable composition; (**d**) Photomicrograph showing Quartz (Qz), plagioclase (Pl) and potash feldspar (Kfs) minerals, sandstone facies; (**e**) Photograph showing sandstone clast incorporated within relatively foliated matrix of Atud tectonized mélange; (**f**) Photomicrograph showing relatively foliated mineral constituents of the Atud tectonized mélange matrix.

The conglomerate lithofacies exhibit variable green, grey and brown colors. They are poorly sorted clast-supported rocks that consist of subrounded to subangular spheroidal to less elliptical lithic fragments of metarhyolite, granodiorite, graphic granite, reworked clastic sediments, carbonates, chert, graphic lithic fragments, spherulitic lithic fragments and andesitic lithic fragments, quartz grains, feldspars (mostly plagioclase), heavy minerals such as zircon and opaques, embedded in a sandy matrix consisting of quartz, feldspars, carbonates and clay minerals (Fig. 11b).

4.1.3. Sandstone lithofacies

The sandstone facies are exposed in the northern part of the Formation, where they are intruded by the metagabbro. It is generally a massive, nonfoliated rock (Fig. 11c). The sandstone is texturally and compositionally sub-mature to immature and petrographically classified as greywacke (El-Lithy, in preparation). The greywacke is made up of two main components: framework grains and cementing materials (matrix and cement). The framework grains are represented mainly by quartz and less frequent feldspar, rare rock fragments, and heavy minerals with or without biotite, all these components being set in a fine-grained matrix (quartz, clay minerals, and sericite) with some carbonate cement (Fig. 11d).

4.2. Atud tectonized mélange

The Atud tectonized mélange is located in the south of the study area. It occurs as scattered poorly-sorted, chaotic, small, low-laying exposures. The rocks are highly weathered, deformed, and relatively foliated, exhibiting green and brown colors. The contact between the Atud tectonized mélange and the Atud formation is unclear, but the fieldwork revealed that the tectonized mélange encloses blocks of the Atud Formation (Fig. 11e), thus it should be deposited sometime later than the Atud Formation. The Atud tectonized mélange consists of exotic and native rock fragments and blocks encircled within a fine-grained sheared and deformed matrix. The large blocks are dominated by blocks of Atud Formation (conglomerates and sandstones), blocks, and mappable lenses of serpentinites and metavolcanics. The pebble-sized lithic fragments consist of metarhyodacite-porphyry, metagreywacke, quartz arenite, granodiorite, andesite and chert. All these lithic fragments are surrounded by a greywacke matrix consisting of quartz, k-feldspar, plagioclase, and clay minerals (Fig. 11f). Dissimilar to clasts within the Atud Formation, the tectonic mélange is characterized by the complete absence of carbonate clasts.

4.3. Metavolcanics

Metavolcanics are compositionally and texturally widely varied. Various metapyroclastics are exposed in the east of the study area along with lava flow. Metapyroclastics are represented meta-agglomerate that are welded manssive greenish-grey rocks. Microscopically, the meta-agglomerate consists of acid lithic fragments and crystal fragments of plagioclase and pyroxene (Fig. 12b). All these constituents are embedded in partially to completely altered fine groundmass.

The lava flows can be separated into acid lava flow and pillow lava. The acid lava flow (metarhyolite porphyry), which outcrops small exposures of medium to low elevations (Fig. 12c). Metarhyolite porphyry exhibits blasto-porphyritic texture (Fig. 12d) and consists of subidioblasts polygonal quartz, highly altered k-feldspars, and minor fine muscovite flakes with fine groundmass rich in quartz, feldspar, muscovite, and fine minute biotite. Garnet, apatite, opaques and zircon present as accessories.

Pillow lava shows an observable spherical to nearly elliptical form in the field (Fig. 12e). It represents medium to fine-grained rocks exhibiting blasto-porphyritic texture and mainly consists of plagioclase, pyroxene, less minor hornblende, serpentine minerals, and chlorite are common alteration products (Fig. 12f). Opaques are common accessories.

4.4. Serpentinites-talc-carbonate

Serpentinites-talc-carbonate rocks are the metamorphic product of the parent ultrabasic members. They are exposed as lenses within the tectonized mélange in the southeastern sector and as a long belt in the west. They are intruded by the metagabbro and are younger than the Atud Formation, as there are no clasts enclosed within the Atud Formation. Petrographically, serpentinites exhibit pseudomorphic mesh texture and glass-hour texture. The serpentinites are primarily composed of serpentine minerals represented by antigorite and chrysotile pseudomorph after olivine and pyroxene (present as relics), carbonate, talc, chromite, and spinel (Fig13b). The talc-carbonate displays pale yellow to white colors and "cavernous and bird nests" structures. They mainly consist of carbonate, talc, and serpentine minerals (Fig. 13c).

4.5. Metagabbro-diorite complex

The metagabbro-diorite complex is considered the youngest rock unit exposed in the northern half of the mapped area and intrude the other rock units. The metagabbro intrudes the Atud Formation at its northern outcrop (Fig. 13c) where xenoliths of the latter are enclosed in the metagabbro. Field and petrographic observation reveal that the metagabbro-diorite differentiates from the hornblende metagabbro in the north outcrops to the diorite southwards. Petrographically, the metagabbro-diorite displays hypidiomorphic granular texture, ophitic and subophitic, and it consists of plagioclase, hornblende, minor tremolite-actinolite and opaque minerals (Fig. 13d).

4.6. Post-metagabbro dykes

The dykes present in the study area only extrude and cut across the metagabbro. The dykes are mostly of acid composition (Fig. 13e) and rare basic to intermediate dykes are recorded as well.

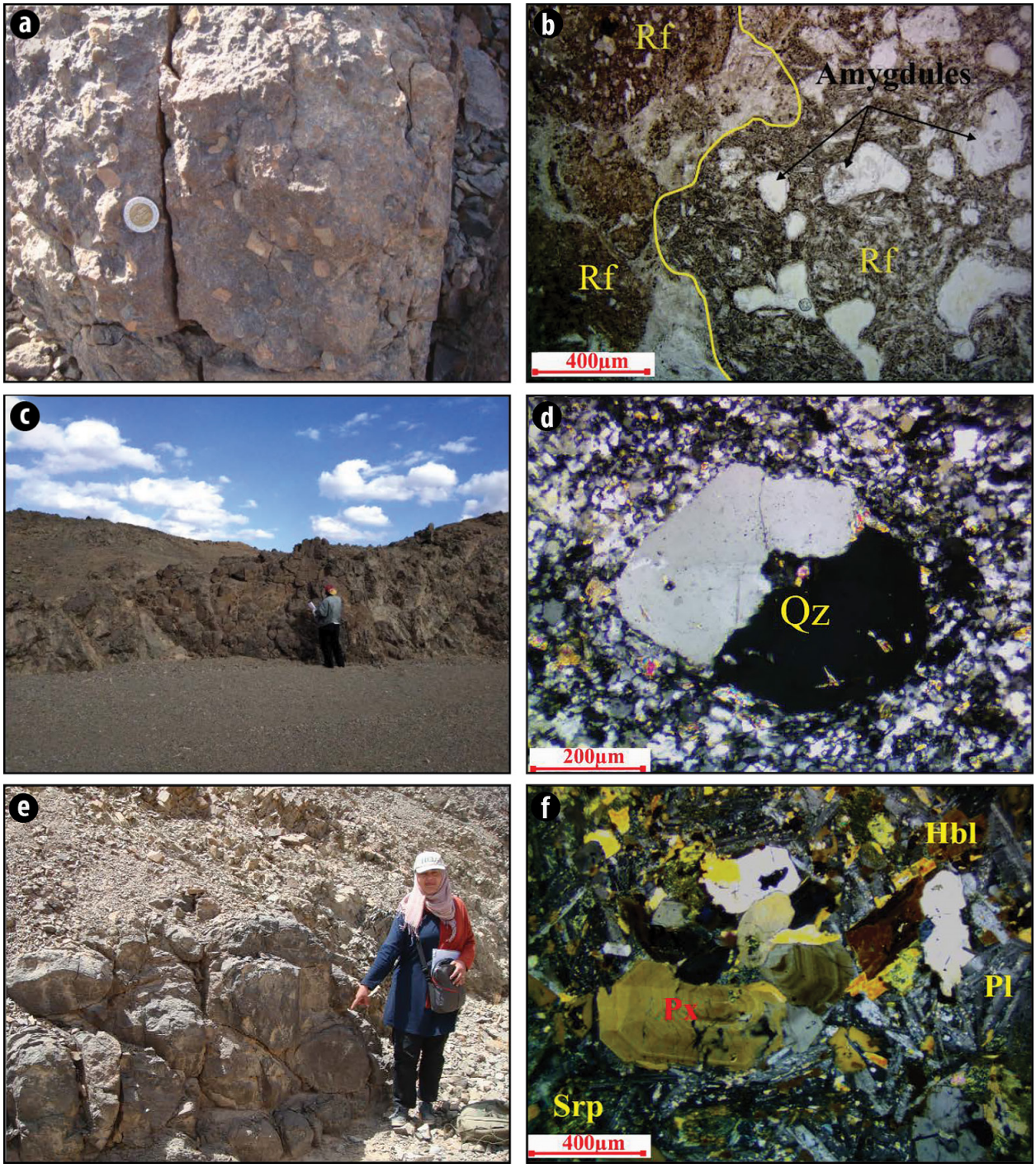

Fig. 12. (**a**) Photograph showing agglomerate mass with angular rock fragments; (**b**) Photomicrograph showing lithic fragments of the agglomerate, PL. (**c**) Photograph showing low elevated acid lava flow; (**d**) Photomicrograph showing twinned quartz (Qz) porphyroblast embedded in fine groundmass, metarhyolite, CN; (**e**) Photograph showing pillow lava; (**f**) Photomicrograph showing zoned pyroxene (Px), plagioclase (Pl), hornblende (Hbl), and serpentinites (Srp) as the mineral constituents of pillow lava, CN.

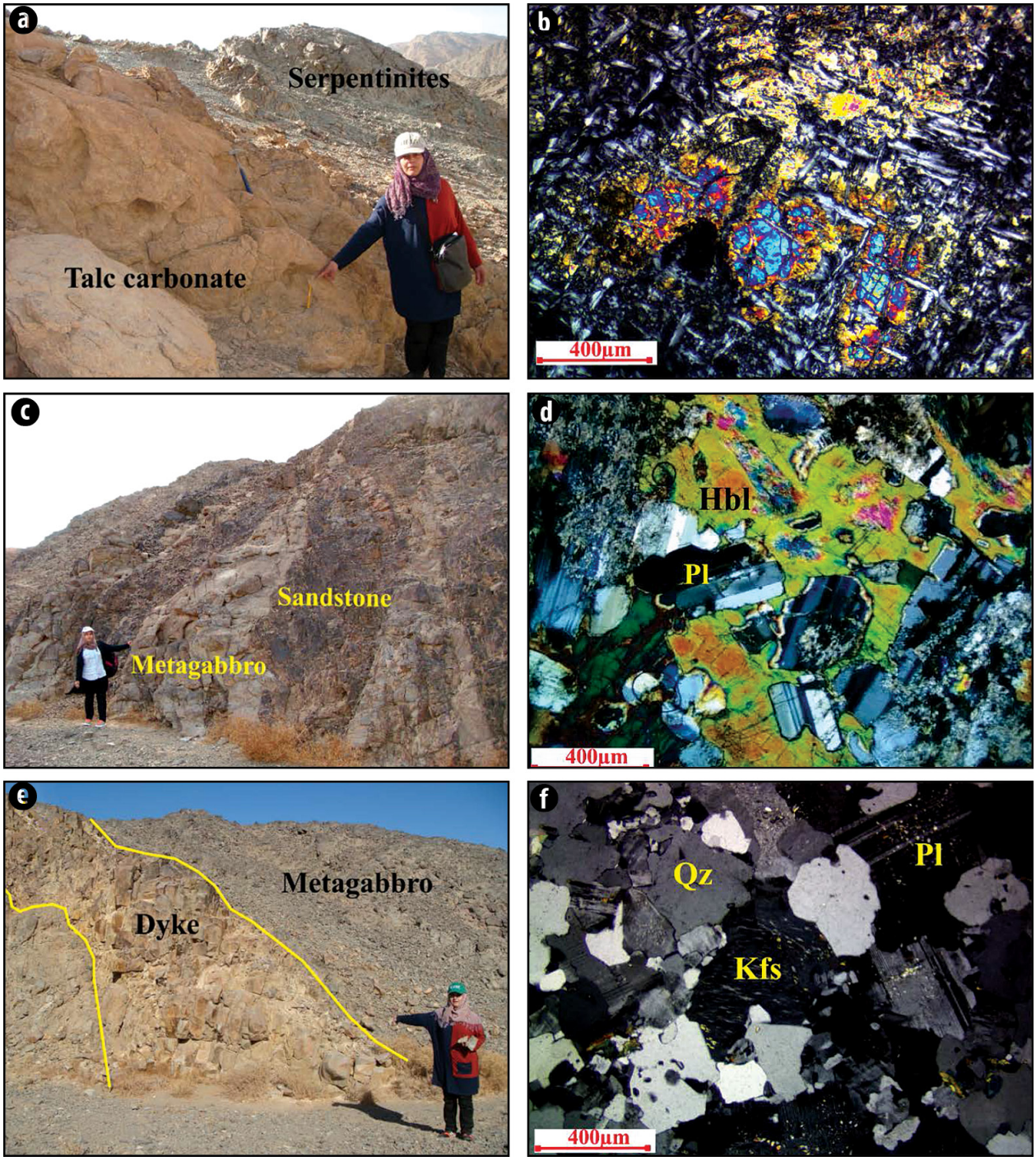

Fig. 13. (**a**) Photograph showing outcrop of serpentinite and talc-carbonate; (**b**) Photomicrograph showing olivine relict altered to serpentine minerals, serpentinites; (**c**) Photograph showing sandstone facies (dark color) of the Atud Formation intruded by the metagabbro (light color); (**d**) Photomicrograph showing ophitic and subophitic textures, metagabbro, C.N; (**e**) Photograph showing rhyolitic dyke extrudes the metagabbro; (**f**) Photomicrograph showing mineral composition of granitic dyke extrudes metagabbro. C.N.

The acid dykes occur as rhyolitic and microgranite dykes. Petrographically, the rhyolite dykes show porphyritic texture and consist of phenocrysts of quartz, k-feldspar and rare plagioclase, all embedded in a fine-grained groundmass. The microgranite dykes exhibit hypidiomorphic granular texture and are mainly composed of quartz, perthite, orthoclase, plagioclase, minor biotite, apatite and opaques (Fig. 13f).

5. CONCLUSION

The utilization of OLI and S2 data in the east of Gabal Atud proved their efficiency in the discrimination of the Atud Formation facies as well as emphasizing the folding and faulting structures of the Atud Formation. The integration of remote sensing images, field observations and earlier geological mapping reveals that the area east of Gabal Atud is covered by the Atud Formation, Atud tectonized mélange, metavolcanics, serpentinites, and their related rocks. All these rock units are intruded by the island-arc metagabbro-metadiorite complex.

The field validation results confirmed that Atud Formation appears as a fantastic large fold in which the beds trend in a curved manner (concave northward) and are folded on themselves at the northeastern periphery of the outcrop.

The sandstone facies highlight the structure (folding and faulting) of the Atud Formation. It can be distinguished for example using the OLI PCA of b1-b2-b3, S2 PCA of (b2), and S2 PCA of b5-b2-b3. Conglomerate facies can be differentiated from the diamictite facies using the band ratio of the S2 (b7/b12) image as the conglomerate has a grey tone compared to the light tone of the diamictite.

Serpentinites-talc-carbonate and diamictite occasionally show similar colors, however, they have different lithological compositions. The differentiation between serpentinites-talc-carbonate rocks and the diamictite is executed from OLI PCA b4-b2- b1, OLI PCA b4-b3- b2, and S2 PCA b5-b2-b3. In addition, the application of band ratio techniques -*e.g.* OLI b6/b7, (b6/b7, b 5/b6, b4/b2), (b4/b6, b5/b6, b6/b7), (b4/b2, b6/b7, b4/b6) and (b6/b7, b7/b3, b6b/5) - prove their ability for lithological discrimination between the serpentinites-talc-carbonate and diamictite. The acid metavolcanics are differentiated from basic metavolcanics and serpentinite, OLI and S2 images including FCC S2 b12-b11-b1, OLI PCA b4 -b3-b2, S2 PCA b5-b2-b3 and OLI band ratio (b4/b2, b6/b7, b4/b6).

REFERENCES

Abdelkader, M.A., Watanabe, Y., Shebl, A., El-Dokouny, H.A., Dawoud, M., Csámer, Á. (2022). Effective delineation of rare metal-bearing granites from remote sensing data using machine learning methods: A case study from the Umm Naggat Area, Central Eastern Desert, Egypt. *Ore Geol. Rev.* **150**, 105184. https://doi.org/10.1016/J.OREGEOREV.2022.105184.

Abdelsalam, M.G., Stern, R.J. (2000). Mapping gossans in arid regions with Landsat TM and SIR-C images, the Beddaho Alteration Zone in northern Eritrea. *J Afr Earth Sci*., **30**(*4*): 903-916.

Abd El-Wahed, M.A., Kamh, S., Ashmawy, M., Shebl, A. (2019). Transgressive structures in the Ghadir Shear Belt, Eastern Desert, Egypt: evidence for partitioning of oblique convergence in the Arabian-Nubian Shield during Gondwana Agglutination. *Acta Geologica Sinica-English Edition*, **93**(*6*): 1614-1646. https://doi.org/10.1111/1755-6724.13882.

Abu El-Ela, F.F. (1990). Do the Atud conglomerates belong to the island arc metasediments? *Bulletin Faculty Science Assiut University, Egypt*, **19**(*1-F*): 123-155.

Abrams, M. J., Brown, D., Lepley, L., Sadowski, R. (1983). Remote sensing for porphyry copper deposits in southern Arizona. *Economic Geology*, **78**(*4*): 591-604.

Akaad, M.K., Essawy, M.A. (1964a). Geology and structure of the area east of Gabal Atud, Eastern Desert, of Egypt. *Bulletin Science Technology Assiut University*, *Egypt*, **7**: 63-83.

Akaad, M.K., Essawy, M.A. (1964b). The metagabbro- diorite complex northeast of Gabal Atud, Eastern Desert, and the term of „epidiorite'. *Bulletin Science Technology Assiut University*, *Egypt*, **7**: 83-108.

Akaad, M.K., Essawy, M.A. (1965a). Petrography, origin, and sedimentation of the Atud Formation and its bearing on the early part of the geological history of the basement complex of the Eastern Desert of Egypt. Bulletin Science Technology Assiut University. *Egypt*, **8**: 55-74.

Ali, K.A., Kröner, A., Hegner, E., Wong, J., Li, S.-Q., Gahlan, H.A., El Ela, F.F. (2015). U-Pb zircon geochronology and Hf-Nd isotopic systematics of Wadi Beitan granitoid gneisses, South Eastern Desert, Egypt. *Gondwana Res*., **27**: 811- 824.

Ali-Bik, M.W., Taman, Z., El Kalioubi, B., Abdel Wahab, W. (2012). Serpentinite-hosted talc-magnesite deposits of Wadi Barramiya area, Eastern Desert, Egypt: characteristics, petrogenesis, and evolution. *J Afr Earth Sci*., **64**: 77-89.

Amin, M.S., Sabet, A.H., Mansour, A.O.S. (1953). Geology of Atud District. Geol. Surv. Egypt, 71 p.

Assiri, A.M. (2016). Remote sensing applications for carbonatite assessment and mapping using VNIR and SWIR bands at Aluyaynah, UAE. Ph.D. Thesis, Michigan State University, 184 p.

Badawi, M., Abd El-atif, M., Shebl, A., Makroum, F., Shalaby, A., Németh, N. (2022). Mapping structurally controlled alterations sparked by hydrothermal activity in the Fatira-Abu Zawal Area, Eastern Desert, Egypt. *Acta Geologica Sinica* (English Edition), **97**(*2*): 662-680.

Barsi, J.A., Lee, K., Kvaran, G., Markham, B.L., & Pedelty, J.A. (2014). The spectral response of the Landsat-8 operational land imager. *Remote Sensing*, **6**(*10*): 10232-10251. https://doi.org/10.3390/rs61010232.

Bates, R.L., Jackson, J.A. (1987). *Glossary of geology*. United States: N. p., Web.

Berkland, J.O., Raymond, L.A., Kramer, J.C., Moores, E.M., O'Day, M. (1972). What is Franciscan? *American Association of Petroleum Geologists Bulletin*, **56**: 2295-2302.

Berman, M., Phatak, A., Traylen, A. (2012). Some invariance properties of the minimum noise fraction transform. *Chemometrics and Intelligent Laboratory Systems*, **117**: 189-199. https://doi.org/10.1016/j.chemolab.2012.02.005.

Chavez, J.P. (1984). Image Processing techniques for Thermatic Mapper data. *Proceedings, ASPRS-ACSM Technical Papers*. **2**: 728-42.

Chavez, P.S., Berlin, GL., Sowers, LB. (1982). Statistical method for selecting Landsat MSS. Thesis, Ph.D. Univ.California, San Diago. *J Appl Photogr Eng*., **8**(*1*): 23-30.

Corumluoglu, O., Vural, A., Asri, I. (2015). Determination of Kula basalts (geosite) in Turkey using remote sensing techniques. *Arab. J. Geosci*., **8**: 10105-10117.

Crosta, A.P., De Souza Filho, C.R., Azevedo, F., Brodie, C. (2003). Targeting key alteration minerals in epithermal deposits in Patagonia, Argentina, using ASTER imagery and principal component analysis. Internat. *J. Remote Sens.*, **24**: 4233-4240.

Dawoud, M., Abdel Ghani, I.M., Elsaid, M., Badr, Y.S. (2017). The integration of ASTER imagery and airborne gamma-ray spectrometry in lithological discrimination of Ras Barud - Um Tagher area, North Eastern Desert, Egypt. *Int J. Innov. Sci., Eng. & Tech.*, **4**(*9*), 9-23.

Dawoud, M., Saleh, G.M., Kamar, M.S., Badr, Y.S., Mahmoud, M. Kh. (2022). Utilization of Landsat-8 OLI Data in the lithological discrimination and mapping of W. El Gemal – W. Sikait area, South Eastern Desert, Egypt. *Int J. Innov. Sci., Eng. & Tech.,* **9**(*8*): 278-309.

Dilek, Y., Festa, A., Ogawa, Y., Pini, G.A. (2012). Chaos and geodynamics: mélanges, mélange-forming processes, and their significance in the geological record. *Tectonophysics*, **568-569**: 1-6. http://dx.doi.org/10.1016/j.tecto.2012.08. 002.

Drury, S.A. (2001). Image interpretation in geology. Nelson Thornes Blackwell Science, Cheltenham Malden, 290 p.

Drusch, M., del Bello, U., Carlier, S., Colin, O., Fernandez, V., Gascon, F., Hoersch, B., Isola, C., Laberinti, P., Martimort, P., Meygret, A., Spoto, F., Sy, O., Marchese, F., Bargellini, P. (2012). Sentinel-2: ESA's Optical High-Resolution Mission for GMES Operational Services. *Remote Sensing of Environment*, **120**: 25-36. https://doi.org/10.1016/J.RSE.2011.11.026

El-Desoky, H.M., Shebl, A., Abdel-Rahman, A.M., Fahmy, W., El-Awny, H., El-Sherif, A.M., El-Rahmany, M.M., Csámer, Á. (2022). Multiscale mineralogical investigations for mineral potentiality mapping of Ras El-Kharit-Wadi Khashir district, Southern Eastern Desert, Egypt. Egypt. *J. Remote Sens. Sp. Sci*. **25**: 941-960. https://doi.org/10.1016/J.EJRS.2022.09.00.1.

El-Lithy, M.A. (In Preparation). The Atud diamictite rocks in the Eastern Desert of Egypt: Implications for the paleogeological processes and paleoclimatology. Ph.D. Thesis, Menoufiya University, Egypt.

El-Magd, I.A., Mohy, H., Basta, F. (2015). Application of remote sensing for gold exploration in the Fawakhir area, Central Eastern Desert of Egypt. *Arab. J. Geosci*., **8**: 3523–3536. https://doi.org/10.1007/s12517-014-1429-4

El-Ramly, M.F., Akaad, M.K. (1960). The basement complex in the Central Eastern Desert of Egypt. Geological Survey, Cairo, Egypt, Paper 8, 35p.

Emam, A., Hamimi, Z., El-Fakharani, A., Abdel-Rahman, E., Barreiro, J.G., Abo-Soliman, M.Y. (2018). Utilization of ASTER and OLI data for lithological mapping of Nugrus-Hafafit area, South Eastern Desert of Egypt. *Arabian Journal of Geosciences*, **11**(*23*). https://doi.org/10.1007/s12517-018-4106-1

Erickson, R. (2011). Petrology of a Franciscan olistostrome with a massive sandstone matrix: The King Ridge Road mélange at Cazadero, California. *Geological Society of America Special Papers*, **480**: 171-188.

Essawy, M.A. (1964). Geology of the area east of Gabal Atud, Eastern Desert. M. Sc. Thesis, Assiut Univ.

Essawy, M.A. (1976). Geochemistry of inhomogeneous rocks from Wadi Mubarak-Gabal Atud, metagabbro- diorite complex, Eastern Desert, Egypt. *The Journal of the University of Kuwait, Science*, **3**: 217.

Eyles, N., Januszczak, N. (2004). 'Zipper-rift': a tectonic model for Neoproterozoic glaciations during the breakup of Rodinia after 750 Ma. *Earth-Science Reviews*, **65**(*1-2*): 1-73. https://doi.org/10.1016/S0012-8252(03)00080-1.

Festa, A., Pini, G.A., Ogata, K., Dilek, Y. (2019). Diagnostic features and field- criteria in recognition of tectonic, sedimentary, and diapiric mélanges in orogenic belts and exhumed subduction-accretion complexes. *Gondwana Research*, **74**: 7-30. https://doi.org/10.1016/J.GR.2019.01.003.

Flint, R.F., Sanders J.E., Rodgers J. (1960). Diamictite, a substitute term symmictite. *Geol Soc Am Bull*., **71**: 1809-1810.

Gaber, S.S., Hassan, S.M., Sadek, M.F. (2015). Prospecting for new gold-bearing alteration zones at El-Hoteib area, South Eastern Desert, Egypt, using remote sensing data analysis. *Ore Geol. Rev.*, **71**: 1-13.

Gad, S., Kusky, T.M. (2006). Lithological mapping in the Eastern Desert of Egypt, the Barramiya area, using Landsat Thematic Mapper (TM). *J. Afr. Earth Sci*., **44**: 196-202.

Gasmi, A., Gomez, C., Zouari, H., Masse, A., Ducrot, D. (2016). PCA and SVM as geo-computational methods for geological mapping in the south of Tunisia, using ASTER remote sensing data set. *Arabian Journal of Geosciences*, **9**(*20*): 753. https://doi.org/10.1007/s12517-016-2791-1.

Gomez, C., Delacourt, C., Allemand, P., Ledru, P., Wackerle, R. (2005). Using ASTER remote sensing data set for geological mapping, in Namibia. *Phys. Chem. Earth*., **30**: 97-108. doi:10.1016/j.pce.2004.08.042.

Green, A.A., Berman, M., Switzer, P., Craig, M.D. (1988). A transformation for ordering multispectral data in terms of image quality with implications for noise removal. *IEEE Trans. Geosci. Remote Sens*., **26**: 65-74.

Irons, J.R., Dwyer, J.L., Barsi, J.A. (2012). The next Landsat satellite: The Landsat data continuity mission. *Remote sensing of environment*, **122**: 11-21.

Khan, S.D., Mahmood, K., Casey, J.F. (2007). Mapping of Muslim Bagh ophiolite complex (Pakistan) using new remote sensing, and field data. *Journal of Asian Earth Sciences*, **30**: 333-343.

Kruse, F.A., Boardman, J.W., Huntington, J.F. (2003). Comparison of airborne hyperspectral data and EO-1 Hyperion for mineral mapping. *IEEE Transactions on Geoscience and Remote Sensing*, **41**: 1388-1400.

Kusky, T.M., Ramadan, T.M. (2002). Structural controls on Neoproterozoic mineralization in the South Eastern Desert, Egypt: an integrated field, Landsat TM, and SIR-C/X SAR approach. *J. Afr. Earth Sci*., **35**(*1*): 107-121.

Langford, R.L. (2015). Temporal merging of remote sensing data to enhance spectral regolith, lithological, and alteration patterns for regional mineral exploration. *Ore Geol. Rev*., **68**: 14-29.

Li, X.H., Abd El-Rahman, Y., Abu Anbar, M., Li, J., Ling, X.X., Wu, L. G., Masoud, A.E. (2018). Old continental crust underlying juvenile oceanic arc: Evidence from Northern Arabian-Nubian Shield, Egypt. Geophysical Res. *Letters*, **45**(*7*): 3001-3008. https://doi.org/10.1002/2018GL077121

Liu, F., Wu, X., Sun, H., Guo, Y. (2007). Alteration information extraction by applying synthesis processing techniques to Landsat ETM+ data: A case study of Zhaoyuan Gold Mines, Shandong Province, China. *J. China Univ. Geosci.*, **18**(*1*): 72-76.

Liu, X., Zhang, B., Gao, L.R., Chen, D.M. (2009). A maximum noise fraction transforms with improved noise estimation for hyperspectral images. *Science in China Series F: Information Sciences 2009*, **52**(*9*): 1578-1587. https://doi.org/10.1007/S11432-009-0156-Z.

Lixin, G., Weixin, X., Jihong, P. (2015). Segmented minimum noise fraction transformation for efficient feature extraction of hyperspectral images. Pattern Recognition, **48**(*10*): 3216–3226. https://doi.org/10.1016/J.PATCOG.2015.04.013.

Loughlin, W.P. (1991). Principal component analysis for alteration mapping. *Photogrammetric Engineering and Remote Sensing*, **57**(*9*): 1163-1169.

Loveland, T.R., Irons, J.R. (2016). Landsat 8: the plans, the reality, and the legacy. *Remote Sens. Environ.* **185**: 1-6.

Mars, J.C., Rowan, L.C. (2006). Regional mapping of phyllic-and argillic-altered rocks in the Zagros magmatic arc, Iran, using Advanced Spaceborne Thermal Emission and Reflection Radiometer (ASTER) data and logical operator algorithms. *Geosphere*, **2**: 161-186.

Ninomiya, Y. (2003). A stabilized vegetation index and several mineralogic indices defined for ASTER VNIR and SWIR data. *In*: IGARSS 2003 IEEE International Geoscience and Remote Sensing Symposium Proceedings (IEEE Cat No03CH37477). IEEE, 1552-1554.

Pearson, K. (1901). Principal components analysis. London, Edinburgh, Dublin Philos. *Mag. J. Sci*., **6**: 559.

Pournamdari, M., Hashim, M., Pour, A.B. (2014). Application of ASTER and Landsat TM data for geological mapping of Esfandagheh Ophiolite Complex, Southern Iran. *Resource Geology*, **64**: 233-246.

Ramadan, T.M., Abdelsalam, M.G., Stern, R.J. (2001). Mapping gold-bearing massive sulfide deposits in the Neoproterozoic Allaqi Suture, Southeast Egypt with Landsat TM and SIR-C/X SAR images. *Photogrammetric Engineering and Remote Sensing*, **67**(*4*): 491-497.

Ranjbar, H., Honarmand, M., Moezifar, Z. (2004). Application of the Crosta technique for porphyry copper alteration mapping, using ETM+ data in the southern part of the Iranian volcanic sedimentary belt. *J. Asian Earth Sci.*, **24**: 237-243.

Richards, J.A. (2012). Remote Sensing Digital Image Analysis: An Introduction, 5th edn. Springer, Canberra, ACT, 494 p.

Rowan, L.C., Hook, S.J., Abrams, M. J., Mars, J. C. (2003). Mapping hydrothermally altered rocks at Cuprite, Nevada, using the Advanced Spaceborne Thermal Emission and Reflection Radiometer (ASTER), a new satellite-imaging system. *Econ. Geol*., **98**: 1019-1027.

Sabine, C. (1999). Remote sensing strategies for mineral exploration. *Remote Sensing for the Earth Sciences – Manuel of Remote Sensing*, 375-447.

Sabins, J., Floyd, F. (1986). Remote sensing: principles and interpretation. Chevron Oil Field Research Co.

Sadek, M.F., Ali-Bik, M.W., Hassan, S.M. (2015). Late Neoproterozoic basement rocks of Kadabora-Suwayqat area, Central Eastern Desert, Egypt: geochemical and remote sensing characterization. *Arab. J. Geosci*., **8**(*12*): 10459-10479.

Schuster, D.C. (1980). The nature and origin of the late Precambrian Gwna mélange, North Wales, United Kingdom [Ph.D. thesis]: Champaign, University of Illinois at Urbana-Champaign, 383 p.

Shebl, A., Abdellatif, M., Hissen, M., Ibrahim Abdelaziz, M., Csámer, Á. (2021). Lithological mapping enhancement by integrating Sentinel 2 and gamma-ray data utilizing support vector machine: A case study from Egypt. *Int. J. Appl. Earth Obs. Geoinf*., **105**, 102619. https://doi.org/10.1016/J.JAG.2021.102619

Shebl, A., Csámer, Á. (2021a). Reappraisal of DEMs, Radar, and optical datasets in lineaments extraction with emphasis on the spatial context. Remote Sens. *Appl. Soc. Environ*., **24**, 100617. https://doi.org/10.1016/J.RSASE.2021.100617

Shebl, A., Csámer, Á. (2021b). Lithological, structural and hydrothermal alteration mapping utilizing remote sensing datasets: a case study around Um Salim area, Egypt. *IOP Conf. Ser. Earth Environ. Sci*., **942**, 012032. https://doi.org/10.1088/1755-1315/942/1/012032

Soliman, M.A., Hegazy, H.A.M. (1989). The Atud Formation, Central Eastern Desert, Egypt – An example of Precambrian slope basin sequence related to a subduction complex. Abst. 27th Annual Meeting, Geol. Soc. Egypt.

Stern, R.J., Ali, K., Asimow, P.D., Azer, M.K., Leybourne, M.I., Mubarak, H.S., Ren, M., Romer, R.L., Whitehouse, M.J. (2020). The atud gabbro–diorite complex: Glimpse of the Cryogenian mixing, assimilation, storage and homogenization zone beneath the Eastern Desert of Egypt. *J. Geol. Soc.*, **177**(*5*): 965-980. https://doi.org/10.1144/jgs2019-199.

Stern, R. J., Avigad, D., Miller, N. R., Beyth, M. (2006). Evidence for the Snowball Earth hypothesis in the Arabian-Nubian Shield and the East African Orogen. *J. Africa. Earth Sci.*, **44**(*1*): 1-20. https://doi.org/10.1016/j.jafrearsci.2005.10.003.

Sultan, M., Arvidson, R.E., Sturchio, N.C. (1986). Mapping of serpentinites in the Eastern Desert of Egypt by using Landsat thematic mapper data. *Geology*, **14**(*12*): 995-999.

van der Meer, F.D., van der Werff, H.M.A., van Ruitenbeek, F.J.A., Hecker, C.A., Bakker, W.H., Noomen, M.F., van der Meijde, M., Carranza, E.J.M., de Smeth, J.B., Woldai, T. (2012). Multi- and hyperspectral geologic remote sensing: A review. *In* International Journal of Applied Earth Observation and Geoinformation, **14**(*1*): 112-128. Elsevier B.V. https://doi.org/10.1016/j.jag.2011.08.002

Xiong,Y., Khan, S.D., Mahmood, K., Sisson, V.B. (2011). Lithological mapping of Bela ophiolite with remote-sensing data. *Int. J. Remote Sens.*, **32**(*16*): 4641-4658.

Yamaguchi, Y., Naito, C. (2003). Spectral indices for lithologic discrimination and mapping by using the ASTER SWIR bands. *Int. J. Remote sens.*, **24**: 4311-4323.

Zhang, X., Pazner, M., Duke, N. (2007). Lithologic and mineral information extraction for gold exploration using ASTER data in the south Chocolate Mountains (California). *ISPRS J. Photogramm Remote Sens.*, **62**(*4*): 271-282.

Zoheir, B., Emam, A. (2012). Integrating geologic and satellite imagery data for high-resolution mapping and gold exploration targets in the South Eastern Desert, *Egypt. J. Afr. Earth Sci.*, **66**: 22-34.